CHEMISTRY OF MATERIALS

pubs.acs.org/cm Article

Ba_2MAsQ_5 (Q = S and Se) Family of Polar Structures with Large Second Harmonic Generation and Phase Matchability

Abishek K. Iyer, Jeong Bin Cho, Michael J. Waters, Jun Sang Cho, Benjamin M. Oxley, James M. Rondinelli, Joon I. Jang,* and Mercouri G. Kanatzidis*

Cite This: https://doi.org/10.1021/acs.chemmater.2c00962 Read Online

ACCESS | Metrics & More | Article Recommendations | Supporting Information

ABSTRACT: Noncentrosymmetric chalcogenides containing stereochemically active lone pair elements, such as As, Sb, and Bi, offer a useful way to tune the band gap and enhance the second harmonic generation (SHG) response. $Ba_2As_{2-x}Sb_xQ_5$, $Ba_2As_{2-x}Bi_xQ_5$ (Q = S and Se), and $Ba_2As_2S_{4.8}Se_{0.2}$ are new chalcoarsenates that crystallize in the noncentrosymmetric monoclinic space group $P2_1$. These five new compounds crystallized with a three-dimensional (3D) $Ba_2As_2Se_5$-type structure, containing AsQ_3 units and $[As_2Q_4]^{2-}$ dimeric units. The $[As_2Q_4]^{2-}$ dimeric unit can be tuned by replacing As with Sb or Bi and Se with S. In contrast, $Ba_2As_2S_5$ crystallizes in the orthorhombic space group $Pca2_1$. Differential thermal analysis suggested that $Ba_2As_2S_5$, $Ba_2As_2Se_5$, $Ba_2AsSbSe_5$, and $Ba_2As_{1.25}Bi_{0.75}Se_5$ melt congruently. The $[M_2Q_4]^{2-}$ unit plays a significant role in tuning the band gap of these compounds, decreasing from 2.02 eV in $Ba_2As_2S_5$ to 1.37 eV in $Ba_2As_{1.25}Bi_{0.75}Se_5$. Powder SHG measurements showed all the compounds are essentially phase-matchable at 3300 nm. $Ba_2AsSbSe_5$ exhibits the highest $\chi^{(2)}$ of 36 pm/V and a laser-induced damage threshold of 0.10 GW/cm^2, comparable to that of $AgGaQ_2$. These materials show significantly improved SHG behavior compared to $BaGa_4Q_7$ compounds, making them attractive for commercial applications.

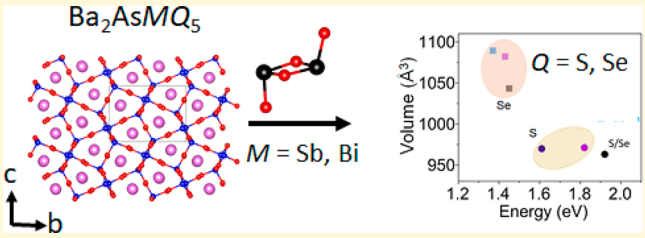

1. INTRODUCTION

The search for new high-performance infrared (IR) nonlinear optical (NLO) materials has motivated research on metal chalcogenides because of their transparency in the IR region, thereby making them preferable over oxides and halides. Hence, they have applications in civil (e.g., medical devices[1] and CO_2 detection[2]) and military (e.g., optical countermeasures[3]) fields. Commercial IR NLO chalcogenide materials, such as $AgGaS_2$, $AgGaSe_2$, and $ZnGeP_2$, show high NLO coefficients, phase matchability, and wide band gap transparency. However, $AgGaQ_2$ (Q = S and Se) suffers from a poor laser-induced damage threshold (LIDT), while $ZnGeP_2$ suffers from 2-photon absorption (2PA).[4−7] The requirements for new practical NLO materials in the IR region are (1) strong SHG response comparable to the benchmark material, $AgGaS_2$, (2) wide transparency in the IR region, (3) high LIDT, (4) phase matchability for good laser output, and (5) congruent melting for large crystal growth. Ideally, the crystals obtained should be environmentally stable.[8−10]

Over the last 15 years, there has been significant progress in the discovery of promising IR NLO materials.[7,8,11−16] Special interest has been focused on the $BaGa_4Q_7$ and $BaGa_2GeQ_6$ (Q = S and Se) systems.[17−20] Reviews by Liang et al.[21] and Luo et al.[7] have discussed the improvement in the crystal quality of these materials over the past decade, which is essential for practical applications. Table 1 shows the experimental SHG coefficients and LIDTs observed from these compounds compared to other commercially used materials detailed in the review by Luo et al.[7] Since the SHG responses of these compounds are comparable to or below that of $AgGaSe_2$, there remains a significant need to search for better materials.

Table 1. Comparison of the Benchmark Materials with Well-Studied Ba-Containing IR NLO Materials[7]

compounds	space group	band gap (eV)	experimental SHG response (pm/V)	LIDT (MW/cm^2)
$AgGaSe_2$	$I\bar{4}2d$	1.8	d_{36} = 39.5	310 (@10 μm)
$ZnGeP_2$	$I\bar{4}2d$	2.0	d_{36} = 75	100
$BaGa_4S_7$	$Pmn2_1$	3.54	d_{32} = 5.7	250
$BaGa_4Se_7$	Pc	2.64	d_{11} = 24	550
$BaGa_2GeS_6$	$R3$	3.23	d_{11} = 26.3	140
$BaGa_2GeSe_6$	$R3$	2.22	d_{11} = 49	110

Alkali (A) and alkaline-earth (AE) metal chalcogen bonds are strongly ionic and play an important role in the electronic

Received: March 29, 2022
Revised: May 2, 2022

structure of solids. The presence of these bonds indirectly plays a role in flattening the band dispersions, thereby increasing the band gap.[22,23] Additionally, elements with stereochemically active lone pairs (SALP) from group 15, such as As, Sb, and Bi, form covalent chalcogen bonds with flexible coordination, which can show second-order Jahn−Teller distortion effects.[24,25] The combination of A/AE metals with SALP-containing elements provides an attractive chemical space to discover noncentrosymmetric chalcogenides. Yan et al.[25] have provided a review of the reported noncentrosymmetric compounds containing group 15 elements. This review suggests that few noncentrosymmetric compounds and even fewer chalcogenides have been reported in the literature. γ-$NaAsSe_2$ has the highest reported SHG response reported to date, which is ∼75 × $AgGaSe_2$. However, it suffers from a phase transition to centrosymmetric δ-$NaAsSe_2$, and it is unstable in air/moisture and is nonphase-matchable in most wavelengths.[26,27] $Ba_{23}Ga_8Sb_2S_{38}$ is the highest-Sb-containing chalcogenide with an SHG response of ∼22 × $AgGaS_2$ at a small particle size.[28] Interestingly, its selenide analogue shows a much weaker response, which is ∼1.7 × $AgGaS_2$.[29] These materials are not phase-matchable. $Cs_5BiP_4Se_{12}$ is one of the few Bi-containing chalcogenides with an SHG response of ∼2 × $AgGaSe_2$.[30]

Chen et al.[31] studied $Ba_2As_2Q_5$ compounds and reported experimental powder SHG responses of ∼1 × $AgGaS_2$ for $Ba_2As_2S_5$ and ∼2.7 × $AgGaS_2$ for $Ba_2As_2Se_5$. Both compounds were reported to be phase-matchable at 2.05 μm and have a higher LIDT than $AgGaS_2$. Interestingly, the analogous $Ba_2Sb_2Se_5$ crystallizes in the centrosymmetric space group *Pbam*.[32] Among the $Ba_2MM'Q_5$ family of compounds reported, where M and M′ are group 13 and 15 elements, respectively, and Q = S, Se, and Te, only two have experimentally noncentrosymmetric structures: Ba_2InBiS_5 and $Ba_2InSbSe_5$ (Table S1). Both compounds showed weak SHG responses.[33,34] $Ba_2InBiTe_5$ was theoretically predicted to have a high $\chi^{(2)}$ value of 98 pm/V but has yet to be experimentally synthesized.[34] All other structures of $Ba_2MM'Q_5$ crystallize with the centrosymmetric Ba_2FeSbS_5 structure containing a cis-$^1/_\infty$ $[MM'Q_5]^{4-}$ unit.[33−37] Table S1 lists all the previously reported $Ba_2MM'Q_5$ compounds. Herein, there are no reported structures where M and M′ are different group 15 elements. There is only one reported quaternary $Cs_3As_2BiS_8$ compound, which undergoes a phase transition from *Pnma* to $P2_1/c$ and a transition to a glass phase.[38]

Driven by the scarcity of the reported structures containing a combination of group 15 elements, we studied the possibility of replacing As with Sb and Bi in $Ba_2As_2Q_5$. We discovered four new compounds, viz., $Ba_2As_{1.25}Sb_{0.75}S_5$, $Ba_2AsSbSe_5$, $Ba_2As_{1.5}Bi_{0.5}S_5$, and $BaAs_{1.25}Bi_{0.75}Se_5$, all of which crystallized with the $Ba_2As_2Se_5$ structure. The ternary $Ba_2As_2S_5$ phase crystallizes in the polar achiral orthorhombic space group $Pca2_1$, while $Ba_2As_2Se_5$ crystallizes in the polar chiral monoclinic space group $P2_1$. We also studied the effect of anion mixing and discovered $Ba_2As_2S_{4.8}Se_{0.2}$, which crystallizes with the $Ba_2As_2Se_5$ structure. The $[M_2Q_4]^{2-}$ unit present in these compounds is the site where As was replaced with Sb and Bi, and S was replaced with Se. The electronic band structure was affected by the elements in the $[M_2Q_4]^{2-}$ unit, which play a critical role in tuning the band gap of these compounds. All the Se compounds melted congruently. Among these compounds, $Ba_2AsSbSe_5$ exhibited the highest SHG response at 3300 nm. All samples were phase-matchable at 3300 nm and have nominal LIDTs, making them highly attractive materials for use in the mid-IR region.

2. EXPERIMENTAL SECTION

2.1. Starting Materials. All manipulations were performed under a dry nitrogen atmosphere in a glovebox. Commercially available BaS (Sigma-Aldrich, 99.95%), As (Alfa Aesar, 99.9%), Sb (Fluka, 99.5%), Bi (American Elements, 99.999%), S (Alfa Aesar, 99.5%), and Se (American Elements, 99.999%) were used as received. BaSe was synthesized via the reaction between elemental Ba and Se. The detailed synthesis of BaSe is provided in the Supporting Information. *Warning: Elemental arsenic was weighed in a glovebox. Precautions were taken in preparing these samples due to their high toxicity.*

2.2. Synthesis of $Ba_2AsSbSe_5$. BaSe (0.499 g; 2.3 mmol), As (0.086 g; 1.1 mmol), Sb (0.140 g; 1.1 mmol), and Se (0.273 g; 3.4 mmol) were loaded in a separate carbon-coated fused-silica tube (13 mm OD, 11 mm ID). The tube was flame-sealed under vacuum (∼3 × 10^{-3} mbar) and inserted in a programmable tube furnace. The temperature of the furnace was increased to 800 °C over 10 h, and annealing was performed at 800 °C for 24 h, followed by cooling to 350 °C for 24 h to obtain a polycrystalline product. Grinding the sample resulted in a dark (gray) $Ba_2AsSbSe_5$ powder. Figure 1 shows

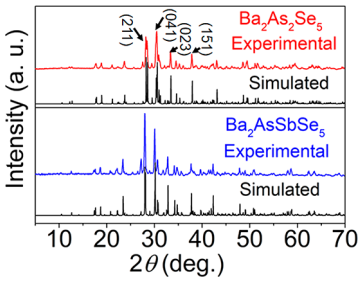

Figure 1. Experimental powder X-ray diffraction of $Ba_2As_2Se_5$ (blue) and $Ba_2AsSbSe_5$ (red) compared to the simulated X-ray diffraction pattern of $Ba_2As_2Se_5$ (black).

the X-ray diffraction (PXRD) pattern for the phase-pure experimental powders. The pattern obtained for $Ba_2AsSbSe_5$ (red) is compared with the experimental (blue) and simulated (black) XRD patterns of $Ba_2As_2Se_5$. Figure S1b shows the results of the SEM/EDS analysis performed on a single crystal of the as-synthesized $Ba_2AsSbSe_5$ compound.

Details of the syntheses of BaSe, $Ba_2As_2S_5$, $Ba_2As_2Se_5$, $Ba_2As_{1.25}Sb_{0.25}S_5$, $Ba_2As_{1.5}Bi_{0.5}S_5$, and $Ba_2As_2S_{4.8}Se_{0.2}$ can be found in the Supporting Information (SI). The SEM/EDS analysis performed on a single crystal of each compound is shown in Figure S1. The experimental PXRD patterns are shown in Figure S2a−c. All the compounds were air-stable for more than 6 months.

2.3. Theoretical SHG Calculations. The density functional theory (DFT) calculations were performed using the Perdew−Burke−Ernzerhof (PBE) functional. The Vienna Ab Initio Simulation Package (VASP) version 5.4.4 was used for structural relaxations and total energy comparisons.[39] GPAW version 21.6.0 was used for the linear and nonlinear optical property calculations.[40] Simulation preparation and postprocessing were performed with Atomic Simulation Environment version 3.22.0.[41] Calculations performed with VASP employed an electronic convergence criterion of a total energy difference of 10^{-8} eV between the electronic iterations and *k*-point grids densities of 20 000 *k*-points per reciprocal Å^3 or greater. Structural relaxations without symmetry constraints were terminated when no forces exceeded 0.5 meV/Å. The plane-wave energy and augmentation grid cut-offs were 550 and 2200 eV, respectively. The structures were resymmetrized to the closest space group and rerelaxed to confirm the space group assignments. The included VASP pseudopotentials were used. Single-point calculations were performed with GPAW before the optical property calculations. The electronic solver convergence criterion had no energy eigenvalue

https://doi.org/10.1021/acs.chemmater.2c00962
Chem. Mater. XXXX, XXX, XXX−XXX

changes greater than 10^{-5} eV between steps. The plane-wave and augmentation grid cutoffs were 600 and 2400 eV, respectively. The *k*-point grid densities were 60 000 k-points per reciprocal $Å^3$ or greater to ensure the convergence of the optical spectra. The linear optical properties were taken from the long-wavelength limit of the dielectric matrix computed with single-particle and random phase approximations. For linear and nonlinear optical calculations, the number of empty bands was increased until the highest empty bands were 20 and 15 eV, respectively, above the conduction band minimum. Both linear and nonlinear optical calculations were performed with scissor shifts to compensate for the difference between the DFT fundamental gap and the experimentally measured band gap.

2.4. Nonlinear Optical Measurements. Crystalline powders of Ba_2AsS_5, $Ba_2As_2Se_5$, $Ba_2AsSbSe_5$, $Ba_2As_{1.25}Sb_{0.75}S_5$, $Ba_2As_{1.5}Bi_{0.5}S_5$, $Ba_2As_{1.25}Bi_{0.75}Se_5$, and $Ba_2As_2S_{4.8}Se_{0.2}$ were provided for NLO characterization after sieving with sizes < 25, 25−53, 53−75, 75−106, 106−150, and >150 μm to examine the phase-matching (PM) behavior, SHG, LIDT, and 2PA coefficient (β) of the samples. Each sample was flame-sealed in a glass capillary tube to prevent exposure to moisture and air and mounted on a homemade sample holder. The SHG efficiencies of the samples were compared with those of the reference material [$AgGaS_2$ ($AgGaSe_2$)] to estimate $\chi^{(2)}$ (LIDT). We could not use $AgGaSe_2$ to characterize $\chi^{(2)}$ because it did not exhibit the correct PM properties, as shown in Figure S3.

The main SHG measurements were performed at room temperature using the input wavelength (λ = 3300 nm) and intensity (0.3 GW/cm^2). We confirmed that this intensity does not induce any noticeable damage to the samples and references because the input wavelength was sufficiently long to ensure that multiphoton absorption (MPA) is minimal, in which the corresponding MPA order is three or four. Therefore, the MPA effect can be neglected in the $\chi^{(2)}$ measurements. Coherent light with a wavelength of 1064 nm was initially produced using an EKSPLA PL-2250 series diode-pumped Nd:YAG laser with a pulse width of 30 ps and a repetition rate of 50 Hz to generate tunable pulses. The Nd:YAG laser pumped an EKSPLA Harmonics Unit (HU) H400, in which the input beam was frequency-tripled to 355 nm using a series of NLO beam mixing. Then, two beams at 355 and 1064 nm entered the EKSPLA PG403-SH-DFG optical parametric oscillator. This oscillator is composed of four main parts: (1) double-pass parametric generator, (2) single-pass parametric amplifier, (3) second harmonic generator (SH), and (4) difference frequency generator (DFG), where the DFG scheme was used to generate the mid-IR (λ = 3300 nm). This wavelength was deliberately selected to ensure that SHG (1650 nm) occurred below the band gap of the samples and references with the same PM behavior. Furthermore, we confirmed that the reported samples were not phase-matchable at λ = 1800 nm (Figure S4). In addition, the LIDT experiment was performed at an excitation wavelength of 1064 nm, a typical wavelength for DFG to generate mid-IR light. Since our samples and reference ($AgGaSe_2$) are optically transparent at 1064 nm, 2PA is the major mechanism for laser-induced damage. The SHG signal was collected using a reflection geometry. Meanwhile, a fiber-optic bundle coupled to a spectrometer equipped with a CCD camera and an InGaAs-based IR detector was used for the LIDT and SHG measurements, respectively. The data collection time was 30 s. A detailed description of our laser and detection setup can be found elsewhere.[42]

3. RESULTS AND DISCUSSION

3.1. Synthetic Details of $Ba_2As_2Q_5$, $Ba_2AsM'Q_5$, $Ba_2As_2S_{4.8}Se_{0.2}$, and BaSe. Pure-phase $Ba_2As_2S_5$ and $Ba_2As_2Se_5$ were obtained at 850 and 800 °C, respectively. Attempts to grow large $Ba_2As_2S_5$ crystals did not result in optical-grade crystals. The synthesis of $Ba_2As_2Se_5$ over slow cooling resulted in a quartz attack, attributable to the presence of BaO in the sample. During the various iterations of this synthesis, we observed the reactive attack of the silica tube when the Ba-oxidized surface was not carefully removed during the synthesis of BaSe. The synthetic details of the BaSe preparation are provided in the SI. The five new non-centrosymmetric compounds, viz., $Ba_2As_2S_{4.8}Se_{0.2}$, $Ba_2As_{1.25}Sb_{0.75}S_5$, $Ba_2AsSbSe_5$, $Ba_2As_{1.5}Bi_{0.5}S_5$, and $Ba_2As_{1.25}Bi_{0.75}Se_5$, crystallized with the $Ba_2As_2Se_5$-type structure (space group: $P2_1$). Pure-phase $Ba_2As_2S_{4.8}Se_{0.2}$, $Ba_2As_{1.25}Sb_{0.75}S_5$, $Ba_2AsSbSe_5$, and $Ba_2As_{1.25}Bi_{0.75}Se_5$ were obtained at 850 °C, while pure $Ba_2As_{1.5}Bi_{0.5}S_5$ was obtained at 950 °C.

3.2. Structural Description of $Ba_2As_2S_5$- and $Ba_2As_2Se_5$-Type Structures. $Ba_2As_2S_5$ crystallizes in the polar achiral space group $Pca2_1$, whereas $Ba_2As_2Se_5$ crystallizes in the polar chiral space group $P2_1$. The crystal structure reported by Cordier et al. exhibited cell constants of a = 17.345(8) Å, b = 9.256(5) Å, and c = 11.946(6) Å in the orthorhombic space group $Pca2_1$.[43] However, our attempts to refine this structure using these lattice parameters were unsuccessful. Successful refinement was obtained when the *a*-axis was doubled, i.e., a = 34.599(7) Å, b = 9.218(8) Å, and c = 11.929(2) Å. The asymmetric unit was composed of 8 Ba atoms, 8 As atoms, and 20 S atoms. A comparison of the simulated and experimental PXRD data is shown in Figure 2a.

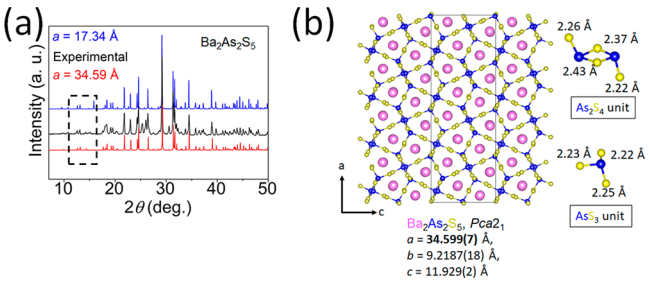

Figure 2. (a) Comparison of the experimental powder X-ray diffraction patterns previously reported (blue) for $Ba_2As_2S_5$ and newly simulated X-ray diffraction data (red). The dashed box shows the peaks missing in the previous data but observed in the experimental data. (b) Crystal structure of $Ba_2As_2S_5$ viewed along the *b*-axis together with the As−S bond lengths of the AsS_3 and $[As_2S_4]^{2-}$ units specified.

Figure 2b shows the crystal structure of $Ba_2As_2S_5$. On the one hand, 4 As atoms are three-coordinated, forming an AsS_3 unit with pyramidal coordination. On the other hand, the other 4 As atoms form an $[As_2S_4]^{2-}$ dimer, where 2 pyramidal AsS_3 units share an edge connected via bridging S_b atoms. The terminal S (S_t) atoms in $[As_2S_4]^{2-}$ are trans to each other, and the 2_1 screw axes pass through the center of the As_2S_4 unit.

Chen et al.[31] have described the structural evolution of $Ba_2As_2Q_5$ from the centrosymmetric $Ba_2GaAsSe_5$ structure containing a $[GaAsSe_5]^{4-}$ unit composed of a trigonal $AsSe_3$ unit and a bridging bond with the $GaSe_4$ unit. Replacing Ga with As results in mirror symmetry, resulting in $[As_2Q_4]^{2-}$ and AsQ_3 units.[31] Figure 3 shows $Ba_2As_2Se_5$, which crystallizes in the monoclinic space group $P2_1$ with cell constants a = 9.476(2) Å, b = 12.36 (3) Å, c = 10.042(2) Å, and β = 117.51(3)°. This structure is consistent with that reported by Cordier et al.[44] Despite the space group difference, both the sulfide and the selenide analogues contain the same basic units with trigonally coordinated AsQ_3 and dimeric $[As_2Q_4]^{2-}$ units. The Ba atoms are coordinated to 6 Q atoms and connected to the adjacent Ba atoms via corner-sharing. Table S2 summarizes the bond lengths of the As−Q bonds in both structures. It

https://doi.org/10.1021/acs.chemmater.2c00962
Chem. Mater. XXXX, XXX, XXX−XXX

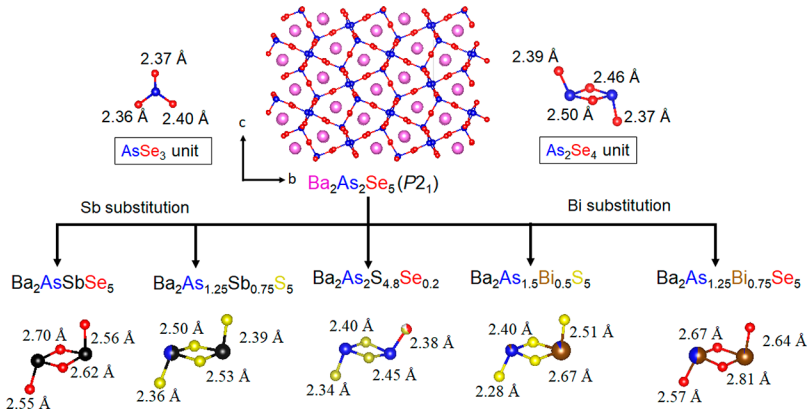

Figure 3. Crystal structure of $Ba_2As_2Se_5$ with the As−Se bond lengths of the $AsSe_3$ and the $[As_2Se_4]^{2-}$ units. The $[M_2Q_4]^{2-}$ units observed in all the new analogues crystallized with the $Ba_2As_2Se_5$-type structure.

Table 2. Crystal data obtained for $Ba_2As_2S_5$, Ba_2AsSbS_5, $Ba_2As_{1.5}Bi_{0.5}S_5$, and $Ba_2As_2S_{4.5}Se_{0.5}$

empirical formula	$Ba_2As_2S_5$	$Ba_2\ As_{1.25}Sb_{0.76}S_5$	$Ba_2As_{1.5}Bi_{0.5}S_5$	$Ba_2As_2S_{4.8}Se_{0.2}$
formula weight	1169.64	621.23	651.85	593.14
temperature	293(2) K			
wavelength	0.71073 Å			
crystal system	orthorhombic	monoclinic	monoclinic	monoclinic
space group	$Pca2_1$	$P2_1$	$P2_1$	$P2_1$
unit cell dimensions	a = 34.567(7) Å, α = 90°	a = 9.2211(18) Å, α = 90°	a = 9.2316(18) Å, α = 90°	a = 9.2442(18) Å, α = 90°
	b = 9.2240(8) Å, β = 90°	b = 12.057(2) Å, β = 117.47(3)°	b = 12.074(2) Å, β = 117.60(3)°	b = 11.989(2) Å, β = 117.52(3)°
	c = 11.920(2) Å, γ = 90°	c = 9.844(2) Å, γ = 90°	c = 9.818(2) Å, γ = 90°	c = 9.797(2) Å, γ = 90°
volume	3800.6(13) Å^3	971.0(4) Å^3	969.0(4) Å^3	963.0(4) Å^3
Z	8	4	4	4
density (calculated)	4.088 g/cm^3	4.249 g/cm^3	4.468 g/cm^3	4.091 g/cm^3
absorption coefficient	16.166 mm^{-1}	15.306 mm^{-1}	23.196 mm^{-1}	16.583 mm^{-1}
F(000)	3612	1088	1132	1045
crystal size	0.5 × 0.14 × 0.12 mm^3	0.014 × 0.012 × 0.01 mm^3	0.13 × 0.11 × 0.11 mm^3	0.22 × 0.19 × 0.16 mm^3
θ range for data collection	2.075 to 33.33°	2.332 to 33.360°	2.341 to 33.320°	2.344 to 29.998°
index ranges	$0 \le h \le 53$, $0 \le k \le 14$, $-18 \le l \le 18$	$-14 \le h \le 14$, $0 \le k \le 17$, $-6 \le l \le 15$	$-14 \le h \le 14$, $-17 \le k \le 18$, $-15 \le l \le 14$	$-14 \le h \le 12$, $-18 \le k \le 18$, $0 \le l \le 15$
reflections collected	7185	3827	12342	5614
independent reflections	7185 [R_{int} = 0.045]	3827 [R_{int} = 0.0283]	6936 [R_{int} = 0.0467]	5614 [R_{int} = 0.0383]
completeness to θ = 25.242°	96.6%	99.5%	100%	100%
refinement method	full-matrix least-squares on F^2			
data/restraints/parameters	7185/0/325	3827/1/166	6936/1/164	5614/1/167
goodness-of-fit	1.001	0.810	1.093	0.974
final R indices [$I > 2\sigma(I)$]	R_{obs} = 0.0347, wR_{obs} = 0.0684	R_{obs} = 0.0312, wR_{obs} = 0.0532	R_{obs} = 0.0527, wR_{obs} = 0.1388	R_{obs} = 0.0536, wR_{obs} = 0.1101
R indices [all data]	R_{all} = 0.0874, wR_{all} = 0.0722	R_{all} = 0.0783, wR_{all} = 0.0582	R_{all} = 0.0728, wR_{all} = 0.1582	R_{all} = 0.1025, wR_{all} = 0.1256
largest diff. peak and hole	1.920 and −2.418 e·Å^{-3}	1.832 and −1.767 e·Å^{-3}	3.861 and −4.718 e·Å^{-3}	1.774 and −1.804 e·Å^{-3}

shows that the larger Se anion (ionic radius: 1.98 Å) in $Ba_2As_2Se_5$ has a larger bond length (average bond length: 2.50 Å in the $[As_2Se_4]^{2-}$ unit, 2.37 Å in the $AsSe_3$ unit) than the S anion (ionic radius: 1.84 Å)[45] in $Ba_2As_2S_5$ (average bond length: 2.40 Å in the $[As_2S_4]^{2-}$ unit, 2.24 Å in the AsS_3 unit).

Table S1 shows all the reported quaternary Ba-containing chalcogenides with compositions of $Ba_2MM'Q_5$, where M is from group 13 (Al, Ga, and In) and M′ is from group 15 (As, Sb, and Bi). Most reported structures crystallize in the centrosymmetric space group *Pnma* with the Ba_2FeSbS_5 structure. In contrast, Ba_2InBiS_5 and $Ba_2InSbSe_5$ crystallize in the noncentrosymmetric space group $Cmc2_1$ but have very low SHG responses.

We studied the effect of replacing As by the larger sized Sb (ionic radius: 0.76 Å) and Bi (ionic radius: 1.03 Å), which belong to the same group as As.[45] All the structures have 2 As atoms and favor the AsQ_3 site, while Sb and Bi favor the $[M_2Q_4]^{2-}$ dimeric unit. Among the compositions, site mixing was not observed only in $Ba_2AsSbSe_5$. Figure 3 summarizes the bond lengths and site occupancies in the $[M_2Q_4]^{2-}$ dimeric unit for all the compounds. The Ba_2AsSbQ_5 (Q = S and Se) structures have 2 As sites that consist of the AsQ_3 unit, while

https://doi.org/10.1021/acs.chemmater.2c00962
Chem. Mater. XXXX, XXX, XXX−XXX

Table 3. Crystal Data Obtained for $Ba_2As_2Se_5$, $Ba_2AsSbSe_5$, and $Ba_2As_{1.25}Bi_{0.75}Se_5$ at 293 K

empirical formula	$Ba_2As_2Se_5$	$Ba_2AsSbSe_5$	$Ba_2As_{1.25}Bi_{0.75}Se_5$
formula weight	819.32	866.15	922.21
wavelength	0.71073 Å		
crystal system	monoclinic		
space group	$P2_1$		
unit cell dimensions	a = 9.4762(19) Å, α = 90°	a = 9.5201(19) Å, α = 90°	a = 9.5468(19) Å, α = 90°
	b = 12.360(3) Å, β = 117.51(3)°	b = 12.522(3) Å, β = 117.45(3)°	b = 12.551(3) Å, β = 117.56(3)°
	c = 10.042(2) Å, γ = 90°	c = 10.227(2) Å, γ = 90°	c = 10.254(2) Å, γ = 90°
volume	1043.1(4) $Å^3$	1081.9(5) $Å^3$	1089.2(5) $Å^3$
Z	4		
density (calculated)	5.217 g/cm^3	5.317 g/cm^3	5.624 g/cm^3
absorption coefficient	31.171 mm^{-1}	29.462 mm^{-1}	39.881 mm^{-1}
$F(000)$	1392	1464	1546
crystal size	0.022 × 0.018 × 0.010 mm^3	0.018 × 0.014 × 0.010 mm^3	0.012 × 0.012 × 0.008 mm^3
θ range for data collection	2.287 to 33.372°	2.244 to 33.322°	2.240 to 33.435°
index ranges	$-14 \le h \le 12, -19 \le k \le 19, 0 \le l \le 15$	$-13 \le h \le 14, -19 \le k \le 19, -15 \le l \le 15$	$-13 \le h \le 14, -19 \le k \le 19, -15 \le l \le 15$
reflections collected	8013	15415	13521
independent reflections	8013 [R_{int} = 0.0321]	8297 [R_{int} = 0.0623]	8322 [R_{int} = 0.0406]
completeness to θ = 25.242°	99.9%	99.9%	100%
refinement method	full-matrix least-squares on F^2		
data/restraints/parameters	8013/1/164	8297/1/164	8322/1/165
goodness-of-fit	0.977	0.903	1.080
final R indices [$I > 2\sigma(I)$]	R_{obs} = 0.0485, wR_{obs} = 0.1156	R_{obs} = 0.0430, wR_{obs} = 0.0700	R_{obs} = 0.0532, wR_{obs} = 0.1312
R indices [all data]	R_{all} = 0.0727, wR_{all} = 0.1278	R_{all} = 0.1067, wR_{all} = 0.0821	R_{all} = 0.0705, wR_{all} = 0.1475
largest diff. peak and hole	2.363 and −3.508 e·$Å^{-3}$	1.863 and −2.375 e·$Å^{-3}$	2.649 and −3.661 e·$Å^{-3}$

independent Sb and mixed Sb/As sites consist of the AsQ_3 unit in $Ba_2As_{1.25}Sb_{0.75}S_5$. The Sb−S bond length in the M_2S_4 unit in $Ba_2As_{1.25}Sb_{0.75}S_5$ ranges from 2.50 to 2.53 Å while the Sb−Se bond length in $Ba_2AsSbSe_5$ ranges from 2.62 to 2.70 Å. This $[Sb_2Q_4]^{2-}$ dimer is a rare motif not observed in other ternary or quaternary Ba−Sb−Q-containing compounds. All such compounds contain an SbQ_3 unit, as observed in $Ba_3Sb_2S_7$,[46,47] or an $[AlSbSe_5]^{4-}$ unit, as observed in $Ba_2AlSbSe_5$.[37] M and M′ in $Ba_2As_{2-x}Bi_xQ_5$ have mixed As and Bi sites for both sulfides and the selenides. $Ba_2As_{1.5}Bi_{0.5}S_5$ contains two independent As sites and an independent As site bonded to a mixed As/Bi site via a bridging sulfide, forming the AsS_3 and M_2S_4 units, respectively. The average bond lengths in the M_2S_4 unit clearly suggest the site preference for the bond formation of Bi (As−S_b) with a bond length of 2.42 Å and As/Bi−S_b with a bond length of 2.66 Å. For the selenide analogue, the only composition obtained was $Ba_2As_{1.25}Bi_{0.75}Se_5$. Here, the $[M_2Se_4]^{2-}$ unit was comprised of a Bi and 50% As/Bi site with the average bond lengths for the As−Se and (As/Bi)−Se bonds being 2.67 and 2.80 Å, respectively.

As mentioned above, $Ba_2As_2S_5$ crystallizes in the $Pca2_1$ space group, whereas $Ba_2As_2Se_5$ crystallizes in the $P2_1$ space group. We investigated the effect of replacing S with the larger Se on the $Ba_2As_2S_5$ structure. We found that 4% Se substitution results in a $Ba_2As_2Se_5$ structure with a formula of $Ba_2As_2S_{4.8}Se_{0.2}$. Similar to Ba_2AsSbQ_5 and $Ba_2As_{2-x}Bi_xQ_5$, site mixing was only observed in the $[As_2Q_4]^{2-}$ unit, as shown in Figure 3. Substitution is preferred at the terminal As−Q bond rather than the bridging As−S bond. The bond length was 2.38 Å on the mixed S/Se site and 2.34 Å on the S site. This tuning of the $[As_2Q_4]^{2-}$ dimer unit offers insight into the versatility of the chemical substitution. Tables 2 and 3 summarize the crystallographic details of the seven compounds studied. The atomic coordinates, detailed atomic displacement values, and bond lengths are listed in Tables S3−23.

3.3. Differential Thermal Analysis (DTA). DTA of the $Ba_2As_2Q_5$, Ba_2AsSbQ_5, and $Ba_2As_{1-x}Bi_xQ_5$ compounds suggests that $Ba_2As_2S_5$, $Ba_2As_2Se_5$, $Ba_2AsSbSe_5$, and $Ba_2As_{1.25}Bi_{0.75}Se_5$ melt congruently. The as-synthesized samples were confirmed to melt congruently upon reheating in a tube furnace under the same reaction conditions. $Ba_2As_2S_5$ (T_m = 688 °C, T_c = 607 °C; Figure 4a) is the only sulfide in its family that melts

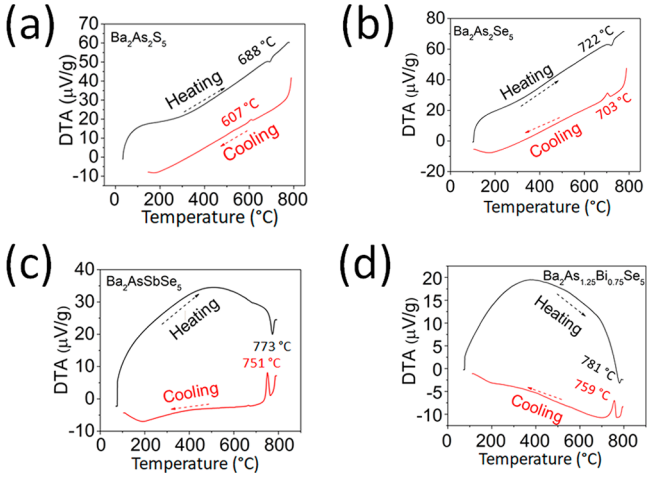

Figure 4. Differential thermal analysis measurements on the congruent melting of (a) $Ba_2As_2S_5$, (b) $Ba_2As_2Se_5$, (c) $Ba_2AsSbSe_5$, and (d) $Ba_2As_{1.25}Bi_{0.75}Se_5$.

congruently. All selenides melt congruently, where the melting and crystallization temperatures of the selenides increase from $Ba_2As_2Se_5$ (T_m = 722 °C, T_c = 703 °C; Figure 4b) to $Ba_2AsSbSe_5$ (T_m = 773 °C, T_c = 751 °C; Figure 4c) to $Ba_2As_{1.25}Bi_{0.75}Se_5$ (T_m = 781 °C, T_c = 759 °C, Figure 4d). A comparison of the PXRD patterns before and after DTA are

https://doi.org/10.1021/acs.chemmater.2c00962
Chem. Mater. XXXX, XXX, XXX−XXX

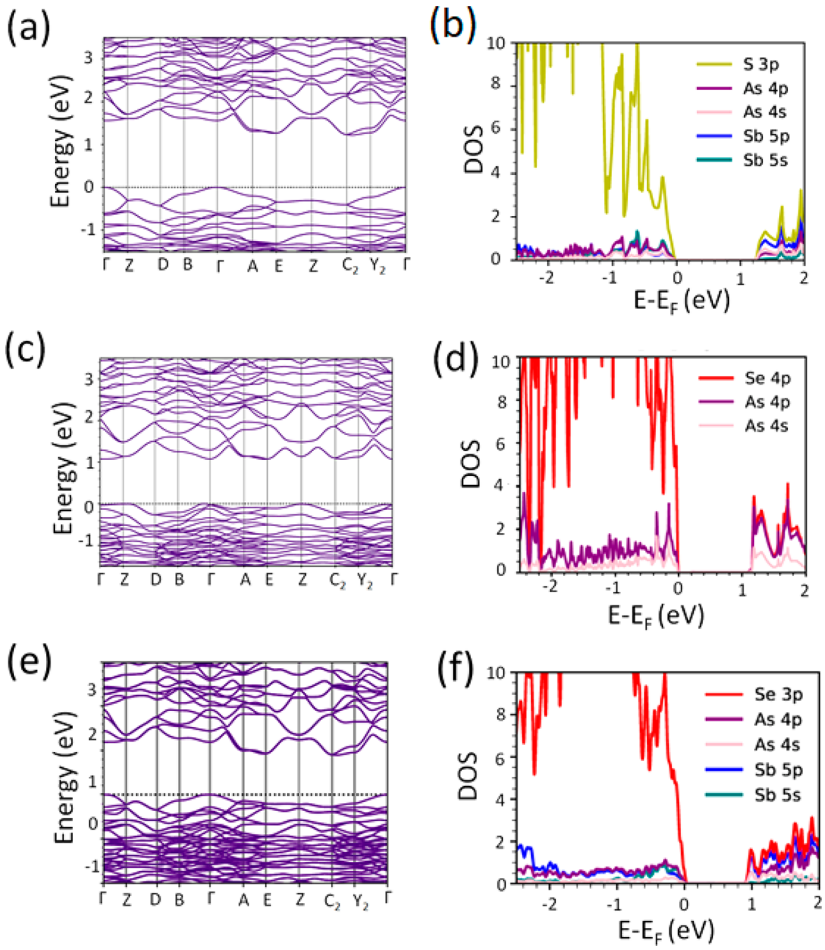

Figure 5. Band structures and density of states (DOS) obtained from the DFT calculations of (a, b) $Ba_2As_{1.25}Sb_{0.75}S_5$, (c, d) $Ba_2As_2Se_5$, and (e, f) $Ba_2AsSbSe_5$, respectively.

shown in Figure S5. For $Ba_2AsSbSe_5$, we see a possible phase transition occurring in both the heating (682 °C) and the cooling (665 °C) curves, but as can be seen in Figure S5d, the PXRD after DTA compares well with the PXRD before DTA. The melting points of all the compounds were lower than those of $BaGa_4S_7$ (T_m = 1090 °C), $BaGa_4Se_7$ (T_m = 1020 °C), $BaGa_2GeS_6$ (908 °C), and $BaGa_2GeSe_6$ (T_m = 880 °C), four families of Ba-containing chalcogenides that have been targeted as promising NLO materials.[7] $Ba_2As_2S_{4.8}Se_{0.2}$ (Figure S6), $Ba_2As_{1.25}Sb_{0.75}S_5$ (Figure S7), and $Ba_2As_{1.5}Bi_{0.5}S_5$ (Figure S8) were found to melt incongruently as confirmed by the PXRD data obtained after DTA and more than one thermal event in the cooling cycle of the experiment.

3.4. Theoretical and Experimental Optical Properties Highlighting the Role of the $[M_2Q_4]^{2-}$ Unit. Chen et al.[31] suggested that As−Q interactions from the AsQ_3 and As_2Q_4 units play an important role in the band gap of $Ba_2As_2S_5$ and $Ba_2As_2Se_5$. Figure 5 compares the band structures of Ba_2AsSbQ_5 (Q = S and Se) and isostructural $Ba_2As_2Se_5$. The valence band (VB) was dominated by the Se *p* states (red curve), and the conduction band (CB) was dominated by the As *p* states, with a smaller contribution from the Se *p* states in $Ba_2As_2Se_5$ (Figure 5b). The VB of Ba_2AsSbQ_5 (Q = S and Se) was dominated mainly by the Q *s* states, while the CB has contributions from the Sb *s* state and Q *p* states (Figure 5d,f). To simplify our calculations, we performed *ab initio* calculations on Ba_2AsSbS_5 instead of $Ba_2As_{1.25}Sb_{0.75}S_5$. The calculated band gaps for $Ba_2As_{1.25}Sb_{0.75}S_5$, $Ba_2As_2Se_5$, and $Ba_2AsSbSe_5$ were 1.2, 1.0, and 0.8 eV, respectively. The contribution of the As and Sb *s* states in the CB clearly indicates that the M_2Q_4 unit plays a significant role in tuning the band gap of these compounds. The band structures of $Ba_2As_{1.25}Sb_{0.75}S_5$, $Ba_2As_2Se_5$, and $Ba_2AsSbSe_5$, shown in Figure 5a,c,e, indicate that they have an indirect band gap with the valence band maximum (VBM) at Γ and conduction band minima (CBM) located at C_2, E, and C_2, respectively. For $Ba_2As_2Se_5$, the VBM was near Γ between Γ and B, while the CBM was at E. $Ba_2As_2S_5$ was found to be a direct band gap material with the VBM and CBM at Γ (Figure S9). The theoretical band gap for $Ba_2As_2S_5$ was found to be 1.45 eV, while the experimental optical band gap was found to be 2.02 eV. We expect a band structure when M = Bi similar to that of Ba_2AsSbQ_5 and expect a contribution from the Bi *s* states in the CB.

The experimental optical band gap measurements performed on ternary $Ba_2As_2Se_5$ and isostructural quaternary $Ba_2As_{1.25}As_{0.75}S_5$, $Ba_2AsSbSe_5$, $Ba_2As_{1.5}Bi_{0.5}S_5$, and $Ba_2As_{1.25}Bi_{0.75}Se_5$ showed a decreased band gap when As was replaced by Sb and Bi in the M_2Q_4 unit for both the sulfides and the selenides (Figure 6a,b). This corroborates with the theoretical calculations that the M_2Q_4 unit plays an important role in tuning the band gap of compounds with this type of structure. The calculated band gaps were underestimated owing to the use of semilocal exchange-correlation functionals.

https://doi.org/10.1021/acs.chemmater.2c00962
Chem. Mater. XXXX, XXX, XXX−XXX

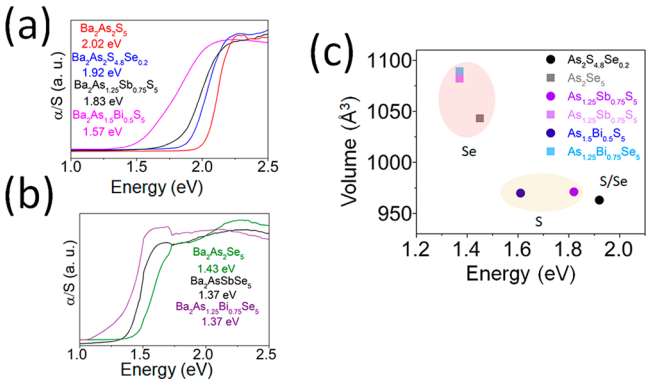

Figure 6. Diffuse reflectance data obtained for (a) $Ba_2As_2S_5$, $Ba_2As_2S_{4.8}Se_{0.2}$, $Ba_2As_{1.25}Sb_{0.75}S_5$, and $Ba_2As_{1.5}Bi_{0.5}S_5$ and (b) $Ba_2As_2Se_5$, $Ba_2AsSbSe_5$, and $Ba_2As_{1.25}Bi_{0.75}Se_5$. (c) Comparison of the band gap (eV) of all the reported compounds with their respective cell volumes (Å^3). The yellow highlighted compounds correspond to sulfides, while the red highlighted compounds correspond to selenides, where the common metal element, Ba, was omitted for convenience.

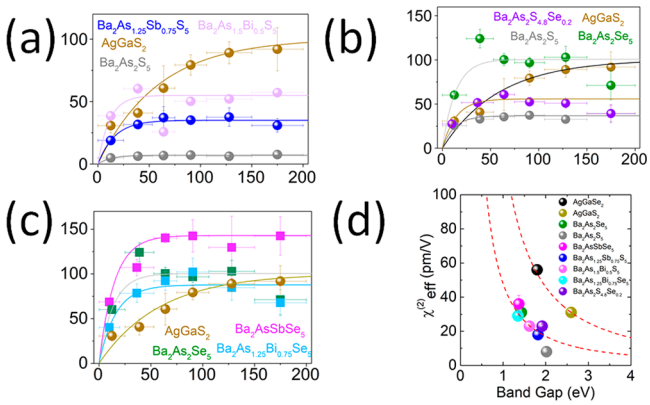

Figure 7. (a, b, c) Phase-matching behavior of all the compounds observed at 3300 nm. Each colored curve is an empirical fit to the data for a guide to the eye. (d) Comparison of the experimentally obtained $\chi^{(2)}$ versus energy band gap (eV) for our samples and $AgGaQ_2$ with slightly different scaling factors that can be different from our samples to the benchmark ternary compounds.

Figure 6c showing the plot of volume versus band gap confirms this trend: from 2.02 eV in $Ba_2As_2S_5$ to 1.62 eV in $Ba_2As_{1.5}Bi_{0.5}S_5$ and 1.45 eV in $Ba_2As_2Se_5$ to 1.37 eV in $Ba_2As_{1.25}Bi_{0.75}Se_5$. Figure 6c shows an inverse relation between the change in volume to the change in the band gap among the sulfides and the selenides. The change in the band gap among the selenides was much less than that of the sulfides, which suggests that the former band gap is much less influenced by Sb and Bi. The black point in the figure shows that the band gap of $Ba_2As_2S_{4.8}Se_{0.2}$ (1.92 eV) falls between the band gaps of $Ba_2As_2S_5$ (2.02 eV) and $Ba_2As_2Se_5$ (1.45 eV). All the compounds were transparent up to 16 μm, making these materials attractive for practical applications in the mid-IR region (Figure S10a−f).

3.5. PM among the $Ba_2As_2Q_5$ and Ba_2AsMQ_5 Compounds (M = Sb and Bi; Q = S and Se). The SHG response of the samples was investigated for the PM behavior at 1800 nm, which is actually the PM onset wavelength for $AgGaS_2$. However, we found that all the compounds were not phase-matchable at this wavelength, as evident from the decreasing SHG counts observed upon increasing the particle size (Figure S4). When compared with the selenide analogues, which show a quick drop in the SHG counts upon increasing the particle size, the sulfides exhibit a slower drop or a larger coherence length, as shown in Figure S4a−f, attributable to the effect of the larger band gaps of the sulfides. For example, the PM onset wavelength for $AgGaS_2$ is 1800 nm, whereas $AgGaSe_2$ has a smaller band gap of 3100 nm.[48]

Figure 7a−c shows the SHG counts of the reference $AgGaS_2$ sample compared to those of $Ba_2As_2Q_5$, $Ba_2As_2S_{4.8}Se_{0.2}$, Ba_2AsSbQ_5, and $Ba_2As_{2-x}Bi_xQ_5$ plotted as a function of particle size at λ = 3300 nm. We found that all the compounds were essentially phase-matchable at 3300 nm. Although the maximum SHGs of $Ba_2As_2Se_5$ (light gray), $Ba_2As_{1.25}Bi_{0.75}Se_5$ (light blue), and $Ba_2As_2S_{4.8}Se_{0.2}$ (black) do not occur at the largest particle size, we can clearly see a transition from a non-PM to a PM behavior when directly comparing the corresponding particle size data at λ = 1800 nm (Figure S4). Therefore, we believe these compounds will exhibit enhanced PM behavior at higher wavelengths. We cannot rule out the possibility that the slight drop in the SHG counts at the largest particle size for these compounds may have resulted from defects and/or inhomogeneity of the samples.

3.6. Nonlinear Susceptibility Measurements at 3300 nm. The second-order susceptibility of each sample ($\chi_S^{(2)}$) was calculated with comparison to $AgGaS_2$ using the Kurtz powder method[42,49] for the PM case.

$$\chi_S^{(2)} = \chi_R^{(2)}\left(\frac{I_S^{SHG}}{I_R^{SHG}}\right)^{1/2} \quad (1)$$

where I_S^{SHG} and I_R^{SHG} are the experimentally measured SHG counts from the test sample and reference, respectively. Using $\chi_R^{(2)}$ ~ 30.5 pm/V for $AgGaS_2$,[42] our calculation yields $\chi_{seff}^{(2)}(Ba_2As_2Se_5)$ ~ 31 ± 3 pm/V, $\chi_{seff}^{(2)}(Ba_2As_2S_5)$ ~ 8 ± 1 pm/V, $\chi_{seff}^{(2)}(Ba_2AsSbSe_5)$ ~ 36 ± 5 pm/V, $\chi_{seff}^{(2)}(Ba_2As_{1.25}Sb_{0.75}S_5)$ ~ 18 ± 2 pm/V, $\chi_{seff}^{(2)}(Ba_2As_{1.5}Bi_{0.5}S_5)$ ~ 23 ± 2 pm/V, $\chi_{seff}^{(2)}(Ba_2As_{1.25}Bi_{0.75}Se_5)$ ~ 29 ± 2 pm/V, and $\chi_{seff}^{(2)}(Ba_2As_2S_{4.8}Se_{0.2})$ ~ 23 ± 1 pm/V at 3300 nm. The theoretical values obtained for $Ba_2As_2Se_5$ at 2050 nm showed the highest tensor component to be d_{14} = 53.6 pm/V, as reported by Chen et al.[31] All the compounds belonged to the two-point group with four independent nonzero d moduli under Kleinman symmetry (d_{14}, d_{16}, d_{22}, and d_{23}). Table 4 shows the calculated d_{14} for $Ba_2As_{1.25}Sb_{0.75}S_5$ = 11.8 pm/V and $Ba_2AsSbSe_5$ = 23.1 pm/V. These values were comparable to the experimentally obtained values.

The linear optical responses for a monoclinic anisotropic system can be obtained using the following equation, $\tilde{n} = n + ik$, where n is the refractive index and k is the extinction coefficient. The extinction coefficient increases once the photon energy exceeds the band gap, as shown in Figure 8. The theoretical birefringence (Δn) of $Ba_2As_{1.25}Sb_{0.75}S_5$ and $Ba_2AsSbSe_5$ was 0.10, as shown in Figure 8. Both compounds show a crossover of n_x and n_y/n_z near 3300 nm, strongly supporting the experimental results that these materials exhibit PM behavior at 3300 nm.

We plotted the $\chi^{(2)}$ values observed for the samples and the reference compounds, $AgGaS_2$ and $AsGaSe_2$, versus the band gap energy (E_g) in Figure 7d on a log−log scale to assess second-order nonlinearity as a function of band gap. The red dashed traces represent the band gap dependence of $\chi^{(2)}$ for the samples and references, which is given by[50]

https://doi.org/10.1021/acs.chemmater.2c00962
Chem. Mater. XXXX, XXX, XXX−XXX

Table 4. Summary of All Reported Non-centrosymmetric $Ba_2AsM'Q_5$ Compounds (M′ = As, Sb, and Bi; Q = S and Se)

compound	space group	volume (Å^3)	band gap (eV)	d_{ij} (pm/V)	$\chi^{(2)}$ (pm/V) (3.3 μm)	LIDT GW/cm^2 (1.064 μm)	T_m (°C)	T_c (°C)
$Ba_2As_2S_5$	$Pca2_1$	3805.3	2.02	d_{33} = 9.9	8 ± 1	0.71 ± 0.07	688	607
$Ba_2As_2S_{4.8}Se_{0.2}$	$P2_1$	963	1.92	not calculated	23 ± 1	0.72 ± 0.07	696	N/A
$Ba_2As_{1.25}Sb_{0.75}S_5$	$P2_1$	971	1.82	d_{14}: 11.91	18 ± 2	0.53 ± 0.05	727	N/A
$Ba_2As_{1.5}Bi_{0.5}S_5$	$P2_1$	969.8	1.57	not calculated	23 ± 2	0.69 ± 0.07	758	N/A
$Ba_2As_2Se_5$	$P2_1$	1043.1	1.45	d_{14}: 53.60	31 ± 3	<0.1	722	703
$Ba_2AsSbSe_5$	$P2_1$	1082	1.43	d_{14}: 23.10	36 ± 5	<0.1	773	751
$Ba_2As_{1.25}Bi_{0.75}Se_5$	$P2_1$	1089.2	1.37	not calculated	29 ± 2	<0.1	781	759

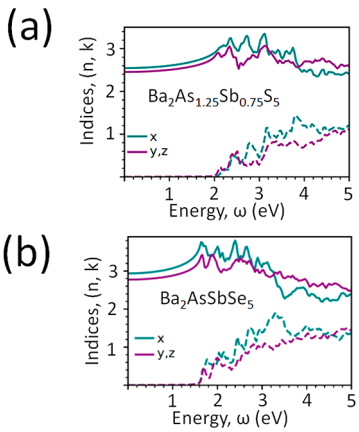

Figure 8. Theoretical dispersion curves obtained for the refractive indices of (a) $Ba_2As_{1.25}Sb_{0.75}S_5$ and (b) $Ba_2AsSbSe_5$. The solid traces correspond to the refractive index (n) along the x-direction (blue) and y, z-directions (purple), and the dashed traces correspond to the imaginary part of the dielectric function, which is the extinction coefficient (k).

$$\chi^{(2)} = a/E_g^{3/2} \tag{2}$$

where a is a scaling parameter to fit our results for $Ba_2MM'Q_5$ (a = 61), $AgGaS_2$, and $AgGaSe_2$ (a = 155). Our results indicate that this simple band gap dependence can be employed to predict the $\chi^{(2)}$ value within the same crystal system but may differ from one material class to another in accordance with the crystal structure, joint density of states, SHG dipole moments, etc. For example, the $\chi^{(2)}$ values observed for ternary diamond-like semiconductors such as $AgGaQ_2$ (Q = S and Se) can be solely explained by their band gap. Likewise, the $\chi^{(2)}$ values observed for the seven chalcoarsenates prepared in our study were reasonably explained by their corresponding band gap values with a single scaling parameter (a = 61), in eq 2.

3.7. Laser-Induced Damage Threshold (LIDT) Measurements at 1064 nm. The SHG counts at a powder diameter (d) in the range of 106−125 μm were measured as a function of input intensity at 1064 nm to assess the LIDT of the samples and reference ($AgGaS_2$) (Figure 9a−h). Since the band gap of $AgGaS_2$ is quite large (2.6 eV) compared to those of the samples, optical damage at this wavelength will occur via three-photon absorption (3PA). Therefore, we deliberately selected $AgGaSe_2$ as the reference, which has a similar band gap (1.8 eV) as the title compounds, which will undergo 2PA at 1064 nm (1.2 eV). The SHG counts proportional to the SHG intensity (I_{SHG}) were fitted using

$$I_{SHG} = b\left(\frac{I}{1 + \beta dI}\right)^2 \tag{3}$$

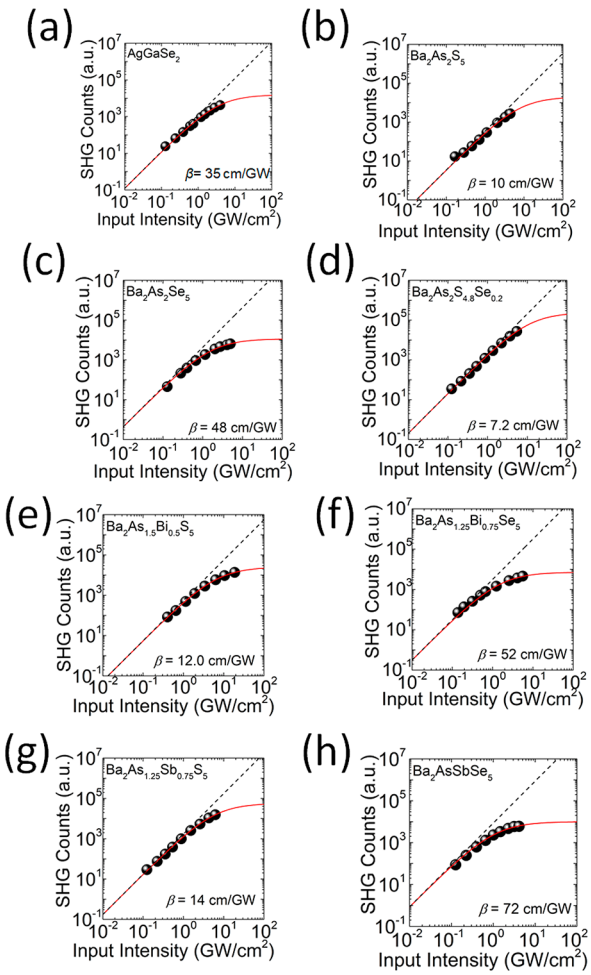

Figure 9. Log−log plots of the SHG counts versus input intensity (I_{input} = 0.1−10 GW/cm^2) obtained for (a) $AgGaSe_2$, (b) $Ba_2As_2S_5$, (c) $Ba_2As_2Se_5$, (d) $Ba_2AsS_{4.8}Se_{0.2}$, (e) $Ba_2As_{1.5}Bi_{0.5}S_5$, (f) $Ba_2As_{1.25}Bi_{0.75}Se_5$ (g) $Ba_2As_{1.25}Sb_{0.75}S_5$, and (h) $Ba_2AsSbSe_5$, respectively, at λ = 1064 nm. The red curve in each plot indicates the best fit using eq 3. The black dashed line corresponds to the case for β = 0.

where I is the fundamental intensity, β is the 2PA coefficient, and b is a proportionality constant that incorporates $\chi^{(2)}$.[51] The experimentally determined β values are tabulated in Table S26, together with other key NLO parameters. Because 2PA is the seed mechanism for optical damage, we estimated LIDT as the intensity at which eq 3 deviates from the black dashed line corresponding to no 2PA in Figure 9. Accordingly, the LIDTs of $AgGaSe_2$, $Ba_2As_2Se_5$, $Ba_2As_2S_5$, $Ba_2AsSbSe_5$, Ba_2AsSbS_5, $Ba_2As_{1.5}Bi_{0.5}S_5$, $Ba_2As_{1.25}Bi_{0.75}Se_5$, and $Ba_2As_2S_{4.8}S_{0.2}$ were 0.24 ± 0.02, 0.10 ± 0.02, 0.71 ± 0.07, 0.10 ± 0.02, 0.53 ± 0.05, 0.69 ± 0.07, 0.10 ± 0.02, and 0.72 ± 0.07 GW/cm^2, respectively.

https://doi.org/10.1021/acs.chemmater.2c00962
Chem. Mater. XXXX, XXX, XXX−XXX

Finally, we used the two-band model, which theoretically predicts $\beta(\omega)$, to verify the band gap dependence of β:[52]

$$\beta(\omega) = K\frac{\sqrt{E_p}}{n_0^2 E_g^3}F_2\left(\frac{\hbar\omega}{E_g}\right) = \frac{K}{\sqrt{95E_g^{5/2}}}F_2\left(\frac{\hbar\omega}{E_g}\right)\ (\mathrm{cm/GW}) \tag{4}$$

where K is the Kane parameter, $E_p \sim 21$ eV is nearly the material-independent energy accounting for the dipole matrix element for typical direct-gap semiconductors, n_0 is the refractive index, and $F_2(x)$ is the 2PA dispersion function, which is given by

$$F_2(x) = \frac{(2x-1)^{3/2}}{(2x)^5} \tag{5}$$

In eq 4, we used the Moss expression[50] to relate the band gap and the refractive index to eliminate the n_0 dependence. To capture the band gap dependence for both the samples and the references, we plotted the dimensionless 2PA coefficients as a function of the band gap in Figure S11 on a log−log scale. The dashed line corresponds to eq 4 plotted to show a theoretical $\beta(E_g)$, where we used K of 4624, an acceptable value depending on the Hamiltonian model calculations.[53] Therefore, our experimental β values were well explained by the band gap energy, a direct consequence of derivatization.

The NLO results are summarized in Table 4 for direct comparison. We believe that the title compounds are promising for beam mixing applications in the mid-IR region. Their possible potential is because of their PM behavior with comparable $\chi^{(2)}$ values and LIDT, comparable with the benchmark IR NLO materials, $AgGaSe_2$ and $AgGaS_2$. Since the NLO properties of the title compounds are well explained by band gap dependence, further derivatization may be employed to maximize the $\chi^{(2)}$ value or LIDT for their individual use but not simultaneously because of the opposite dependence on E_g.

4. CONCLUSIONS

$Ba_2As_{1.25}Sb_{0.75}S_5$, $Ba_2AsSbSe_5$, $Ba_2As_{1.5}Bi_{0.5}S_5$, and $Ba_2As_{1.25}Bi_{0.75}Se_5$ adopted a $Ba_2As_2Se_5$ structure and featured polar structures. $Ba_2As_2S_5$ crystallizes in the orthorhombic space group ($Pca2_1$), whereas $Ba_2As_2Se_5$ crystallizes in the monoclinic space group ($P2_1$). The effect of anion (Q) substitution, with just 4% Se, resulted in a new mixed-anion compound, $Ba_2As_2S_{4.8}Se_{0.2}$, which crystallizes in the $Ba_2As_2Se_5$ structure. These compounds are composed of AsQ_3 trigonal pyramidal units. The main units of substitution are the molecular M_2Q_4 anion, where M = As/Sb in $Ba_2As_{2-x}Sb_xQ_5$ and M = As/Bi in $Ba_2As_{2-x}Bi_xQ_5$, and the terminal M−Q bond in $Ba_2As_2S_{4.8}Se_{0.2}$. All compounds were phase-matchable at 3300 nm, which was confirmed using *ab initio* calculations. $Ba_2AsSbSe_5$ exhibited the highest experimental $\chi^{(2)}$ value of 36 ± 5 pm/V among the selenides, while $Ba_2As_{1.5}Bi_{0.5}S_5$ exhibited the highest experimental $\chi^{(2)}$ value of 23 ± 1 pm/V among the sulfides. The sulfides have a high LIDT ($Ba_2As_2S_5$, 0.71 ± 0.07 GW/cm^2, 1064 nm), while all the selenides have lower LIDTs of 0.10 ± 0.02 GW/cm^2 at 1064 nm. The selenide compounds melt congruently, which is necessary for growing large crystals of these compounds using melt processing. These compounds have higher SHG and LIDT responses than those observed for the $BaGa_4Q_7$ family of compounds, making them highly attractive for further development as IR NLO materials.

■ ASSOCIATED CONTENT

Supporting Information

The Supporting Information is available free of charge at https://pubs.acs.org/doi/10.1021/acs.chemmater.2c00962.

Experimental methods and physical property measurements; X-ray crystallographic tables of the atomic coordinates, displacement parameters, selected bond lengths, and bond angles of $Ba_2As_2S_5$,$Ba_2As_2Se_5$, $Ba_2As_{1.25}Sb_{0.75}S_5$, $Ba_2AsSbSe_5$, $Ba_2As_{1.5}Bi_{0.5}S_5$, $Ba_2As_{1.25}Bi_{0.75}Se_5$, and $Ba_2As_2S_{4.8}Se_{0.2}$; PXRD patterns obtained from all the produced materials; DTA of $Ba_2As_{1.25}Sb_{0.75}S_5$, $Ba_2As_{1.5}Bi_{0.5}S_5$, and $Ba_2As_2S_{4.8}Se_{0.2}$; PXRD before and after DTA of $Ba_2As_2S_5$, $Ba_2As_2Se_5$, $Ba_2As_{1.25}Sb_{0.75}S_5$, $Ba_2AsSbSe_5$, $Ba_2As_{1.5}Bi_{0.5}S_5$, $Ba_2As_{1.25}Bi_{0.75}Se_5$, and $Ba_2As_2S_{4.8}Se_{0.2}$; optical absorption data for all the produced materials; particle size dependence of all the produced compounds; band structure of $Ba_2As_2S_5$; SHG intensity of all the produced compounds at λ = 1800 nm; and plots with the 2PA coefficient for all the produced compounds (PDF)

■ AUTHOR INFORMATION

Corresponding Authors

Mercouri G. Kanatzidis − *Department of Chemistry, Northwestern University, Evanston, Illinois 60208, United States;* orcid.org/0000-0003-2037-4168; Email: m-kanatzidis@northwestern.edu

Joon I. Jang − *Department of Physics, Sogang University, Seoul 04107, South Korea;* orcid.org/0000-0002-1608-8321; Email: jjcoupling@sogang.ac.kr

Authors

Abishek K. Iyer − *Department of Chemistry, Northwestern University, Evanston, Illinois 60208, United States;* orcid.org/0000-0002-8582-3895

Jeong Bin Cho − *Department of Physics, Sogang University, Seoul 04107, South Korea*

Michael J. Waters − *Department of Materials Science and Engineering, Northwestern University, Evanston, Illinois 60208, United States*

Jun Sang Cho − *Department of Physics, Sogang University, Seoul 04107, South Korea*

Benjamin M. Oxley − *Department of Chemistry, Northwestern University, Evanston, Illinois 60208, United States*

James M. Rondinelli − *Department of Materials Science and Engineering, Northwestern University, Evanston, Illinois 60208, United States;* orcid.org/0000-0003-0508-2175

Complete contact information is available at: https://pubs.acs.org/10.1021/acs.chemmater.2c00962

Notes

The authors declare no competing financial interest.

The cif files for the reported compounds can be found deposited in the CSD. Below are the numbers corresponding to the structures: CSD number for $Ba_2As_2S_5$, 2162314; CSD number for $Ba_2As_{1.25}Sb_{0.75}S_5$, 2162315; CSD number for $Ba_2AsSbSe_5$, 2162316; CSD number for $Ba_2As_2S_{4.8}Se_{0.2}$, 2162317; CSD number for $Ba_2As_{1.25}Bi_{0.75}Se_5$, 2162318; CSD number for $Ba_2As_{1.5}Bi_{0.5}S_5$, 2162319; CSD number for $Ba_2As_2Se_5$, 2162320.

■ ACKNOWLEDGMENTS

M.G.K., A.K.I, and B.M.O. acknowledge the Air Force Office of Scientific Research Grant Number FA9550-18-S-0003. The IMSERC PCM facility at Northwestern University used in this work received support from the Soft and Hybrid Nanotechnology Experimental (SHyNE) Resource (NSF ECCS-2025633), and Northwestern University. The computational work by J.M.R and M.J.W. was supported by the National Science Foundation (NSF) Grant No. DMR-2011208. Access to facilities for high-performance computing resources at Northwestern University is acknowledged. J.I.J. acknowledges the support of the Basic Science Research Programs (2020R1F1A1069646 and 2021R1A2C2013625) through the National Research Foundation of Korea (NRF), funded by the Korean government. M.J.W. would like to thank Anubhab Haldar for his performance enhancing patches to GPAW.

■ REFERENCES

(1) Garmire, E. Nonlinear optics in daily life. *Opt Express* **2013**, *21*, 30532−30544.

(2) Pushkarsky, M. B.; Webber, M. E.; Macdonald, T.; Patel, C. K. N. High-sensitivity, high-selectivity detection of chemical warfare agents. *Appl. Phys. Lett.* **2006**, *88* (4), 044103.

(3) Tholl, H. D. *Review and prospects of optical countermeasure technologies*; SPIE: 2018; Vol. *10797*.

(4) Boyd, R. W. *Nonlinear Optics*, 3rd ed.; Elsevier: 2008; pp 1−613.

(5) Schunemann, P. G.; Schepler, K. L.; Budni, P. A. Nonlinear frequency conversion performance of $AgGaSe_2$, $ZnGeP_2$, and $CdGeAs_2$. *MRS Bull.* **1998**, *23* (7), 45−49.

(6) Nikogosyan, D. N. *Nonlinear Optical Crystals: A Complete Survey*, 1st ed.; Springer: New York, NY, 2005; p XII, *428*.

(7) Luo, X.; Li, Z.; Guo, Y.; Yao, J.; Wu, Y. Recent progress on new infrared nonlinear optical materials with application prospect. *J. Solid State Chem.* **2019**, *270*, 674−687.

(8) Chung, I.; Kanatzidis, M. G. Metal Chalcogenides: A Rich Source of Nonlinear Optical Materials. *Chem. Mater.* **2014**, *26* (1), 849−869.

(9) Liang, F.; Kang, L.; Lin, Z.; Wu, Y. Mid-Infrared Nonlinear Optical Materials Based on Metal Chalcogenides: Structure−Property Relationship. *Cryst. Growth & Design* **2017**, *17* (4), 2254−2289.

(10) Zhang, W.; Yu, H.; Wu, H.; Halasyamani, P. S. Phase-Matching in Nonlinear Optical Compounds: A Materials Perspective. *Chem. Mater.* **2017**, *29* (7), 2655−2668.

(11) Guo, S.-P.; Chi, Y.; Guo, G.-C. Recent achievements on middle and far-infrared second-order nonlinear optical materials. *Coord. Chem. Rev.* **2017**, *335*, 44−57.

(12) Li, Z.; Yao, J.; Wu, Y. Chalcophosphates: A Treasure House of Infrared Nonlinear Optical Materials. *Cryst. Growth & Design* **2020**, *20* (11), 7550−7564.

(13) Kang, L.; Liang, F.; Jiang, X.; Lin, Z.; Chen, C. First-Principles Design and Simulations Promote the Development of Nonlinear Optical Crystals. *Acc. Chem. Res.* **2020**, *53* (1), 209−217.

(14) Isaenko, L. I.; Yelisseyev, A. P. Recent studies of nonlinear chalcogenide crystals for the mid-IR. *Semicond. Sci. Technol.* **2016**, *31* (12), 123001.

(15) Wu, K.; Yang, Y.; Gao, L. A review on phase transition and structure-performance relationship of second-order nonlinear optical polymorphs. *Coord. Chem. Rev.* **2020**, *418*, 213380.

(16) Ohmer, M. C.; Pandey, R. Emergence of Chalcopyrites as Nonlinear Optical Materials. *MRS Bull.* **1998**, *23* (7), 16−22.

(17) Lin, X.; Zhang, G.; Ye, N. Growth and Characterization of BaGa4S7: A New Crystal for Mid-IR Nonlinear Optics. *Cryst. Growth Design* **2009**, *9* (2), 1186−1189.

(18) Yao, J.; Mei, D.; Bai, L.; Lin, Z.; Yin, W.; Fu, P.; Wu, Y. BaGa4Se7: A New Congruent-Melting IR Nonlinear Optical Material. *Inorg. Chem.* **2010**, *49*, 9212−9216.

(19) Lin, X.; Guo, Y.; Ye, N. BaGa2GeX6(X = S, Se): New mid-IR nonlinear optical crystals with large bandgaps. *J. Solid State Chem.* **2012**, *195*, 172−177.

(20) Yin, W.; Feng, K.; He, R.; Mei, D.; Lin, Z.; Yao, J.; Wu, Y. BaGa2MQ6 (M = Si, Ge; Q = S, Se): a new series of promising IR nonlinear optical materials. *Dalton Trans.* **2012**, *41*, 5653−5661.

(21) Liang, F.; Kang, L.; Lin, Z.; Wu, Y.; Chen, C. Analysis and prediction of mid-IR nonlinear optical metal sulfides with diamond-like structures. *Coord. Chem. Rev.* **2017**, *333*, 57−70.

(22) Bera, T. K.; Song, J. H.; Freeman, A. J.; Jang, J. I.; Ketterson, J. B.; Kanatzidis, M. G. Soluble direct-band-gap semiconductors $LiAsS_2$ and $NaAsS_2$: large electronic structure effects from weak As···S interactions and strong nonlinear optical response. *Angew. Chem., Int. Ed. Engl.* **2008**, *47* (41), 7828−7832.

(23) Song, J.-H.; Freeman, A. J.; Bera, T. K.; Chung, I.; Kanatzidis, M. G. First-principles prediction of an enhanced optical second-harmonic susceptibility of low-dimensional alkali-metal chalcogenides. *Phys. Rev. B* **2009**, *79* (24), 245203.

(24) Hu, C.; Zhang, B.; Lei, B. H.; Pan, S.; Yang, Z. Advantageous Units in Antimony Sulfides: Exploration and Design of Infrared Nonlinear Optical Materials. *ACS Appl. Mater. Interfaces* **2018**, *10* (31), 26413−26421.

(25) Yan, M.; Xue, H.-G.; Guo, G.-C. Recent Achievements in Lone-Pair Cation-Based Infrared Second-Order Nonlinear Optical Materials. *Cryst. Growth & Design* **2021**, *21*, 698−720.

(26) Bera, T. K.; Jang, J. I.; Song, J.-H.; Malliakas, C. D.; Freeman, A. J.; Ketterson, J. B.; Kanatzidis, M. G. Soluble Semiconductors $AAsSe_2$ (A = Li, Na) with a Direct-Band-Gap and Strong Second Harmonic Generation: A Combined Experimental and Theoretical Study. *J. Am. Chem. Soc.* **2010**, *132*, 3484−3495.

(27) He, J.; Iyer, A. K.; Waters, M. J.; Sarkar, S.; Zu, R.; Rondinelli, J. M.; Kanatzidis, M. G.; Gopalan, V. Giant Non-Resonant Infrared Second Order Nonlinearity in γ -NaAsSe2. *Adv.Opt. Mater.* **2022**, *10* (2), 2101729.

(28) Chen, M. C.; Wu, L. M.; Lin, H.; Zhou, L. J.; Chen, L. Disconnection enhances the second harmonic generation response: synthesis and characterization of Ba23Ga8Sb2S38. *J. Am. Chem. Soc.* **2012**, *134* (14), 6058−6060.

(29) Yin, W.; Zhou, M.; Iyer, A. K.; Yao, J.; Mar, A. Noncentrosymmetric quaternary selenide Ba23Ga8Sb2Se38: Synthesis, structure, and optical properties. *J. Alloys Compd.* **2017**, *729*, 150−155.

(30) Chung, I.; Song, J.-H.; Jang, J. I.; Freeman, A. J.; Ketterson, J. B.; Kanatzidis, M. G. Flexible Polar Nanowires of Cs5BiP4Se12 from Weak Interactions between Coordination Complexes: Strong Nonlinear Optical Second Harmonic Generation. *J. Am. Chem. Soc.* **2009**, *131*, 2647−2656.

(31) Chen, M.-M.; Ma, Z.; Li, B.-X.; Wei, W.-B.; Wu, X.-T.; Lin, H.; Zhu, Q.-L. M2As2Q5 (M = Ba, Pb; Q = S, Se): a source of infrared nonlinear optical materials with excellent overall performance activated by multiple discrete arsenate anions. *J. Mater. Chem. C* **2021**, *9* (4), 1156−1163.

(32) Wang, J.; Lee, K.; Kovnir, K. Synthesis, crystal structure, and thermoelectric properties of two new barium antimony selenides: Ba2Sb2Se5and Ba6Sb7Se16.11. *J. Mater. Chem. C* **2015**, *3* (38), 9811−9818.

(33) Geng, L.; Cheng, W. D.; Lin, C. S.; Zhang, W. L.; Zhang, H.; He, Z. Z. Syntheses and characterization of new mid-infrared transparency compounds: centric Ba2BiGaS5 and acentric Ba2BiInS5. *Inorg. Chem.* **2011**, *50* (12), 5679−5686.

(34) Lin, C.-S.; Luo, Z.-Z.; Cheng, W.-D.; Zhang, H.; Zhang, W.-L. Design of SHG materials with mid-infrared transparency based on genetic engineering for Ba2BiInA5 (A = Se, Te). *J. Mater. Chem.* **2012**, *22* (40), 21713−21719.

(35) Li, C.; Li, X.; Huang, H.; Yao, J.; Wu, Y. Ba2AsGaSe5: A New Quaternary Selenide with the Novel [AsGaSe5](4-) Cluster and Interesting Photocatalytic Properties. *Inorg. Chem.* **2015**, *54* (20), 9785−9789.

(36) Wu, X.; Gu, X.; Pan, H.; Hu, Y.; Wu, K. Synthesis, Crystal Structures, Optical Properties and Theoretical Calculations of Two Metal Chalcogenides Ba2AlSbS5 and Ba2GaBiSe5. *Crystals* **2018**, *8* (4), 165.

(37) Wu, X.; Gu, X.; Pan, H.; Hu, Y.; Wu, K. Synthesis, Crystal Structures, Optical Properties and Theoretical Calculations of Two Metal Chalcogenides Ba2AlSbS5 and Ba2GaBiSe5. *Crystals* **2018**, *8*, 165−175.

(38) Bera, T. K.; Iyer, R. G.; Malliakas, C. D.; Kanatzidis, M. G. Crystalline and glassy phases in the Cs/Bi/As/S system. *Inorg. Chem.* **2013**, *52* (19), 11370−11376.

(39) Kresse, G.; Furthmüller, J. Efficient iterative schemes for ab initio total-energy calculations using a plane-wave basis set. *Condens. Matter Mater. Phys.* **1996**, *54* (16), 11169−11186.

(40) Romero, A. H.; Allan, D. C.; Amadon, B.; Antonius, G.; Applencourt, T.; Baguet, L.; Bieder, J.; Bottin, F.; Bouchet, J.; Bousquet, E.; Bruneval, F.; Brunin, G.; Caliste, D.; Côté, M.; Denier, J.; Dreyer, C.; Ghosez, P.; Giantomassi, M.; Gillet, Y.; Gingras, O.; Hamann, D. R.; Hautier, G.; Jollet, F.; Jomard, G.; Martin, A.; Miranda, H. P. C.; Naccarato, F.; Petretto, G.; Pike, N. A.; Planes, V.; Prokhorenko, S.; Rangel, T.; Ricci, F.; Rignanese, G.-M.; Royo, M.; Stengel, M.; Torrent, M.; van Setten, M. J.; Van Troeye, B.; Verstraete, M. J.; Wiktor, J.; Zwanziger, J. W.; Gonze, X. , ABINIT: Overview, and focus on selected capabilities. *J. Chem. Phys.* **2020**, *152*, 124102.

(41) Larsen, A. H.; Mortensen, J. J.; Blomqvist, J.; Castelli, I. E.; Christensen, R.; Dułak, M.; Friis, J.; Groves, M. N.; Hammer, B.; Hargus, C.; Hermes, E. D.; Jennings, P. C.; Jensen, P. B.; Kermode, J.; Kitchin, J. R.; Kolsbjerg, E. L.; Kubal, J.; Kaasbjerg, K.; Lysgaard, S.; Maronsson, J. B.; Maxson, T.; Olsen, T.; Pastewka, L.; Peterson, A.; Rostgaard, C.; Schiøtz, J.; Schütt, O.; Strange, M.; Thygesen, K. S.; Vegge, T.; Vilhelmsen, L.; Walter, M.; Zeng, Z.; Jacobsen, K. W. The Atomic Simulation Environment—A Python library for working with atoms. *J. Phys.: Condens. Matter* **2017**, *29*, 273002.

(42) Brant, J. A.; Clark, D. J.; Kim, Y. S.; Jang, J. I.; Weiland, A.; Aitken, J. A. Outstanding Laser Damage Threshold in Li_2MnGeS_4 and Tunable Optical Nonlinearity in Diamond-Like Semiconductors. *Inorg. Chem.* **2015**, *54* (6), 2809−2819.

(43) Cordier, G.; Schwidetzky, C.; Schaefer, H. Darstellung und Struktur von Ba2As2S5. *Inorg. Chem. React.* **1983**, *20*, 877−883.

(44) Cordier, G.; Schwidetzky, C.; Schaefer, H. Darstellung und Struktur von Ba2As2Se5. *Inorg. Chem. React.* **1985**, *22*, 93−100.

(45) Shannon, R. D. Revised Effective Ionic Radii and Systematic Studies of Interatomie Distances in Halides and Chaleogenides. *Acta Crystallogr. A* **1976**, *32*, 751−767.

(46) Geng, L.; Luo, Z.-Z.; Cheng, W.-D. A new Sb-based polysulfide: Ba3Sb2S7 containing (S2)2− ligand. *J. Mol. Struct.* **2013**, *1048*, 482−486.

(47) Wang, J.; Lee, K.; Kovnir, K. Synthesis, Crystal, and Electronic Structure of Ba3Sb2Q7(Q = S,Se). *Z. Anorg. Allg. Chem.* **2015**, *641* (6), 1087−1092.

(48) Aitken, J. A.; Brant, J. A.; Clark, D. J.; Kim, Y. S.; Jang, J. I. Impact of bandgap on infrared optical nonlinearity in novel quaternary chalcogenides: Cu2CdSnS4, α/ β-Cu2ZnSiS4 and Li2CdSnS4. In *Nonlinear Optics: Fundamentals, Applications and Technological Advances*; Wilkins, F., Ed.; NOVA Scientific Publishers: New York, 2014; p 224.

(49) Brant, J. A.; Clark, D. J.; Kim, Y. S.; Jang, J. I.; Zhang, J.-H.; Aitken, J. A. Li2CdGeS4, A Diamond-Like Semiconductor with Strong Second-Order Optical Nonlinearity in the Infrared and Exceptional Laser Damage Threshold. *Chem. Mater.* **2014**, *26* (10), 3045−3048.

(50) Jackson, A. G.; Ohmer, M. C.; LeClair, S. R. Relationship of the second order nonlinear optical coefficient to energy gap in inorganic non-centrosymmetric crystals. *Infrared Physics & Technology* **1997**, *38*, 233−244.

(51) Zhang, J.-H.; Clark, D. J.; Brant, J. A.; Rosmus, K. A.; Grima, P.; Lekse, J. W.; Jang, J. I.; Aitken, J. A. α-Li2ZnGeS4: A Wide-Bandgap Diamond-like Semiconductor with Excellent Balance between Laser-Induced Damage Threshold and Second Harmonic Generation Response. *Chem. Mater.* **2020**, *32* (20), 8947−8955.

(52) Sheik-Bahae, M.; Hutchings, D. C.; Hagan, D. J.; Van Stryland, E. W. Dispersion of bound electronic nonlinear refraction in solids. *IEEE J. Quantum Electron.* **1991**, *27*, 1296−1309.

(53) Jang, J. I.; Park, S.; Clark, D. J.; Saouma, F. O.; Lombardo, D.; Harrison, C. M.; Shim, B. Impact of two-photon absorption on second-harmonic generation in CdTe as probed by wavelength-dependent Z-scan nonlinear spectroscopy. *J. Opt. Am. Soc.* **2013**, *30*, 2292−2295.

https://doi.org/10.1021/acs.chemmater.2c00962
Chem. Mater. XXXX, XXX, XXX−XXX